

On the Relationship between Thermodynamic Structure and Cloud Top, and Its Climate Significance in the Arctic

JOSEPH SEDLAR

Remote Sensing Division, Research Department, Swedish Meteorological and Hydrological Institute, Norrköping, Sweden

MATTHEW D. SHUPE

Cooperative Institute for Research in Environmental Sciences, University of Colorado, and NOAA/ESRL/PSD, Boulder, Colorado

MICHAEL TJERNSTRÖM

Department of Meteorology, Stockholm University, and Bert Bolin Centre for Climate Research, Stockholm, Sweden

(Manuscript received 4 April 2011, in final form 18 August 2011)

ABSTRACT

Cloud and thermodynamic characteristics from three Arctic observation sites are investigated to understand the collocation between low-level clouds and temperature inversions. A regime where cloud top was 100–200 m above the inversion base [cloud inside inversion (CII)] was frequently observed at central Arctic Ocean sites, while observations from Barrow, Alaska, indicate that cloud tops were more frequently constrained to inversion base height [cloud capped by inversion (CCI)]. Cloud base and top heights were lower, and temperature inversions were also stronger and deeper, during CII cases. Both cloud regimes were often decoupled from the surface except for CCI over Barrow. In-cloud lapse rates differ and suggest increased cloud-mixing potential for CII cases.

Specific humidity inversions were collocated with temperature inversions for more than 60% of the CCI and more than 85% of the CII regimes. Horizontal advection of heat and moisture is hypothesized as an important process controlling thermodynamic structure and efficiency of cloud-generated motions. The portion of CII clouds above the inversion contains cloud radar signatures consistent with cloud droplets. The authors test the longwave radiative impact of cloud liquid above the inversion through hypothetical liquid water distributions. Optically thin CII clouds alter the effective cloud emission temperature and can lead to an increase in surface flux on the order of 1.5 W m^{-2} relative to the same cloud but whose top does not extend above the inversion base. The top of atmosphere impact is even larger, increasing outgoing longwave radiation up to 10 W m^{-2} . These results suggest a potentially significant longwave radiative forcing via simple liquid redistributions for a distinctly dominant cloud regime over sea ice.

1. Introduction

Clouds are ubiquitous over the Arctic, especially during the summer half of the year when cloud occurrence can be as large as 80%–90% (Herman and Goody 1976; Curry and Ebert 1992; Wang and Key 2005; Shupe et al. 2011). Both shortwave and longwave radiation are modified by cloud–radiative interactions (e.g., Curry et al. 1996), affecting the energy budgets at both the surface and top of atmosphere (TOA). Cloud droplets reflect and absorb

shortwave radiation, resulting in surface cooling, and absorb and reemit longwave radiation, resulting in a warming at the surface—the cloud “greenhouse” effect. The magnitudes of surface cloud warming and cooling are dependent upon the solar zenith angle, surface albedo, and the cloud micro- and macrophysical characteristics (Curry and Ebert 1992; Curry 1995; Minnett 1999; Intrieri et al. 2002a; Shupe and Intrieri 2004; Sedlar et al. 2011). For most of the year, clouds warm the surface in the Arctic (Intrieri et al. 2002a; Shupe and Intrieri 2004; Dong et al. 2010). Changing cloud and sea ice characteristics in a changing climate will likely impact the cloud–radiative interaction.

Temperature inversions are also ubiquitous in the lower Arctic atmosphere. They occur frequently in the lowest few hundred meters above ground level (AGL)

Corresponding author address: Joseph Sedlar, Remote Sensing Division, Research Department, Swedish Meteorological and Hydrological Institute, Norrköping, Sweden.
E-mail: joseph.sedlar@smhi.se

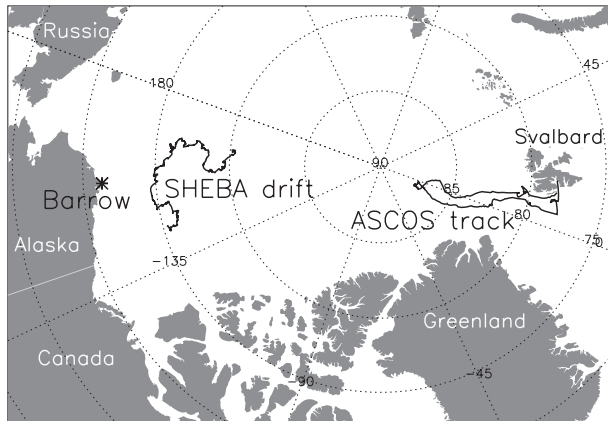


FIG. 1. Geographic distribution of the Barrow observatory, the SHEBA drift track, and the ASCOS track.

throughout all seasons (Kahl 1990; Curry et al. 1996; Tjernström and Graversen 2009). Low-level temperature inversions are most persistent and strongest during the winter months when surface solar heating is minimal or absent (Kahl 1990; Liu et al. 2006; Tjernström and Graversen 2009; Devasthale et al. 2010). These structures result from a combination of local processes, such as radiative cooling and cloud distribution, as well as large-scale processes, such as subsidence and meridional heat and moisture transport (e.g., Curry et al. 1996). Inversions provide a local layer of static stability and can impact vertical transport.

To first order, cloud characteristics are determined by the state of the local thermodynamics. In the same way, clouds feed back to the thermodynamics via diabatic processes, such as latent heating and radiative divergence. Paluch and Lenschow (1991) describe how the convection of turbulent entrainment and cloud-top radiative cooling can “adjust” potential temperature inversions above the tops of marine stratiform clouds. Longwave radiative cooling is generally dominant over shortwave absorption heating near cloud top. The magnitudes, however, vary based on cloud phase, optical depth, and cloud-droplet effective size (Herman and Goody 1976; Curry 1986). Therefore, the net radiative cooling of a cloud top in the vicinity of a temperature inversion could increase the static stability across the inversion base. This distinct thermodynamic relationship between Arctic cloud top and the temperature inversion is the object of this study.

In contrast to the prototypical inversion-capping structure of subtropical stratiform clouds (Paluch and Lenschow 1991; Klein and Hartmann 1993; Tjernström and Rune 2003), Sedlar and Tjernström (2009) identified a regime of low-level central Arctic clouds where cloud-top heights derived from S-band radar were found above

the temperature inversion base height. During their month-long campaign near the North Pole, such a regime was observed more than twice as often as the prototypical capped stratiform-cloud regime. Liquid is often present in Arctic stratiform-cloud layers (Herman and Goody 1976; Intrieri et al. 2002b; Shupe 2011), and liquid water content in these clouds tends to have a maximum near cloud top (e.g., Tsay and Jayaweera 1984). Therefore, cloud tops protruding into the temperature inversion may have a significant effect on the cloud microphysical composition, lifetime, and the radiative forcing, as well as the thermodynamic structure itself. Curry (1983) modeled the significance of cloud condensate within a temperature inversion for the development of continental polar air masses, however the authors are unaware of additional detailed analyses on Arctic cloud tops and inversion structures. Since the cloud inversion relationship over the Arctic has not been examined, except in Sedlar and Tjernström (2009), a number of questions remain open-ended. What processes lead to formation and persistence of a cloud layer inside the temperature inversion? Do the thermodynamics permit the cloud layer above the inversion or does the cloud modify the thermodynamics to support cloud existence in the stable layer? Is there a moisture source above the temperature inversion base? An understanding of the occurrence frequency and mechanisms supporting such a cloud regime is necessary and is the motivation for this study.

This paper examines the relationship between temperature inversions and clouds below 3 km in the Arctic. Cloud and thermodynamic properties from three Arctic observational locations are examined to address the frequency of cloud tops extending into the inversion structure, as identified by Sedlar and Tjernström (2009). We examine the cloud and thermodynamic characteristics between regimes to understand potential processes that may enhance the occurrence of one regime over the other. In addition, radiative transfer calculations are used so as to understand possible radiative effects associated with clouds extending into the inversion. Finally, a discussion and a summary of the main results and key processes impacting Arctic cloud regimes are provided.

2. Data and instruments

Detailed observations of cloud and thermodynamic structure in the Arctic for long time periods are difficult to obtain. We use observations from three sites (Fig. 1): the Department of Energy North Slope of Alaska (NSA) site in Barrow, Alaska, the Surface Heat Budget of the Arctic Ocean (SHEBA) drifting ice camp (Uttal et al. 2002), and the Arctic Summer Cloud–Ocean Study

(ASCOS) cruise and drifting ice camp (Sedlar et al. 2011). All three sites have nearly identical instrumentation. Both ice camp datasets provide insight into central Arctic Ocean cloud and thermodynamic properties, potentially more influenced by sea ice on a seasonal time scale. These data record lengths are relatively short: one full year for SHEBA and approximately one late summer month for ASCOS at different latitudes. Data from 2003 to 2008 at Barrow are used and therefore provide the only longer, quasi-climatological perspective on clouds and thermodynamics. Barrow is located on the coast with continental, marine, and sea ice influences. Data used by Sedlar and Tjernström (2009) are not examined here owing to differing instrumentation. However, their data and analysis on cloud and inversion relationships provided the framework for the more spatial and temporal analysis here.

All remote sensing instruments used are surface based and vertically pointing, described in detail in Shupe et al. (2005). All data have undergone strict quality-control measures. Millimeter Cloud Radar (MMCR) (Moran et al. 1998) observations are used to identify vertical cloud boundaries upward from 105 m AGL, the height of the lowest radar range gate. While designed to detect cloud droplets, it is possible that low concentrations of small droplets may not be sensed. The vertical range gate resolution is 45 m and sampling is every 10 s. Cloud boundaries were determined using the Active Remote Sensing of Cloud Layers algorithm (Clothiaux et al. 2000) with a slightly more demanding threshold applied here. Only cloud layers spanning a thickness greater than 135 m (three vertical range gates) with a top below 3 km AGL are analyzed. Cloud base is estimated using ceilometer and/or micropulse lidar measurements at 20-s time resolution; if these observations are unavailable, the MMCR is used to determine the cloud base but is often biased low due to precipitation. The ceilometer–lidar estimate generally identifies the lowest vertical location of liquid water and becomes increasingly attenuated as cloud optical thickness increases. Dual-channel microwave radiometers (MWR) provide vertically integrated liquid water path (LWP) with a retrieval uncertainty of $\pm 25 \text{ g m}^{-2}$ (e.g., Westwater et al. 2001).

Thermodynamic profiles are analyzed from radiosoundings at each site. These range from approximately four times daily during the ASCOS drift to twice and often only once daily with intermittent time gaps during the SHEBA drift and at Barrow. Thermodynamic profiles were interpolated to 10-m vertical resolution. Temperature inversions are identified using thresholds applied to the temperature profile. An inversion thickness more than 40 m and a minimum of 40 m between

successive inversions are required for inclusion in the statistics and analysis. Inversions not passing these thresholds are ignored from analysis. Specific humidity profiles are examined to identify specific humidity inversions, hereafter referred to as moisture inversions, coinciding with analyzed temperature inversions.

Median cloud boundaries are computed from 10-min data following each radiosounding release. We assume that the median cloud layers are in steady state over the 10-min window, a reasonable assumption for persistent low-level Arctic stratus clouds (Shupe et al. 2011). However, the relatively high frequency remote-sensor-determined cloud boundaries often varied by one or more range gates within this window. Thus, median rather than mean boundaries are analyzed, reducing the influence of outlier cloud boundaries within the time window. For example, such averaging errors could occur when a single cloud layer transitions to a multilayered system. The median cloud boundaries are compared with the corresponding radiosounding thermodynamic profile. Only cases when a median cloud top and a temperature inversion coincided vertically and in proximity to each other are included in the analysis. Multiple inversions are observed below 3 km AGL, but the algorithms employed identify a cloud–inversion collocation if and only if the median cloud base is vertically above the inversion base, which must be, at a minimum, 40 m above the subsequent inversion top. We focus our analysis on the two cloud–inversion regimes identified in Sedlar and Tjernström (2009), namely cloud tops capped by inversion base and cloud tops above inversion base.

3. Cloud properties

a. Cloud–inversion regimes

The cloud–thermodynamic regimes are distinguished as 1) median cloud-top height at or below the inversion-base height by no more than 100 m [classified as cloud capped by inversion (CCI)] and 2) median cloud-top height at least 90 m above inversion-base height but below inversion-top height [classified as cloud inside inversion (CII)]. A CII must therefore extend a minimum of two radar range gates above the inversion-base height to be included in the analysis. Any cloud layers not satisfying these thresholds, or those above 3000 m AGL, are ignored. We qualitatively show the relationship between cloud layer and collocated temperature inversion for a CCI case (Figs. 2a,b) and a CII case (Figs. 2c,d) observed during the ASCOS drift. Cloud radar reflectivity shows depth of the cloud layer, including hydrometeors falling from the cloud layer. The geometrical thin CCI case shows a median cloud top at 780 m AGL with a median

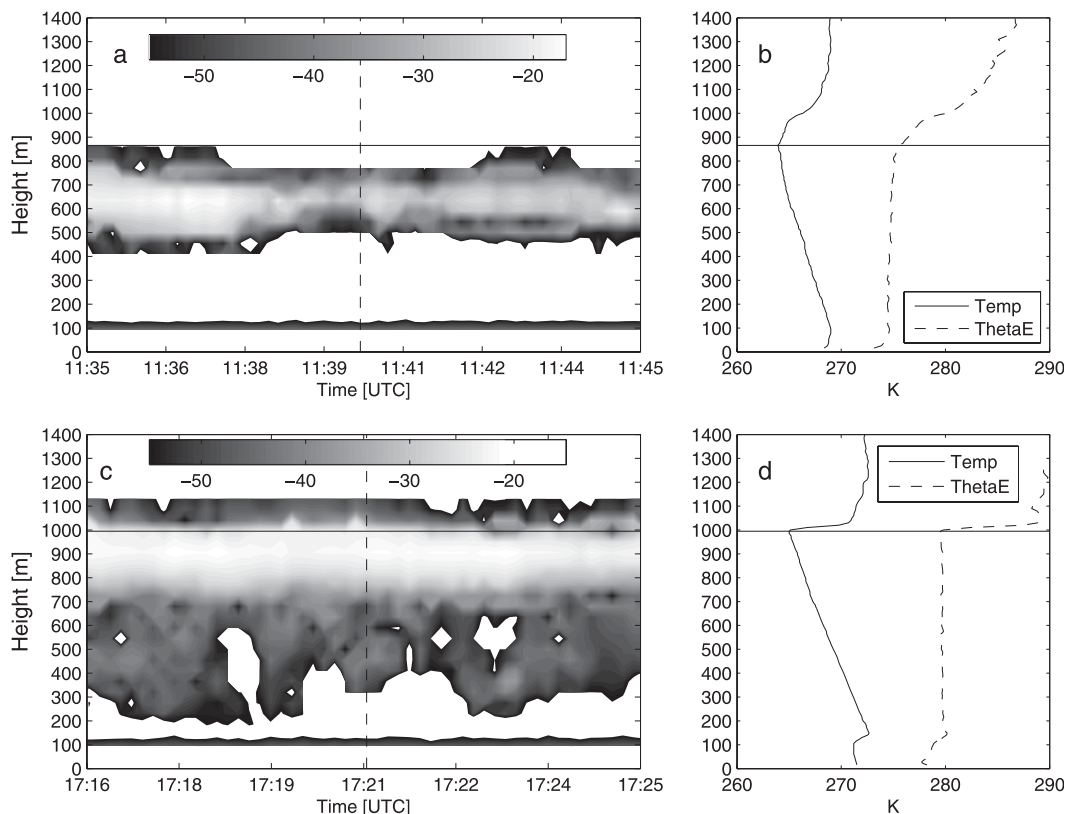


FIG. 2. Qualitative look at the cloud top-temperature inversion collocations for two observed cases during the ASCOS drift, (top) CCI and (bottom) CII: (a) cloud and precipitation reflectivity contours (dBZ; grayscale bar) for 10 min around 1140 UTC 31 Aug 2008, showing (b) temperature (solid line) and equivalent potential temperature (dashed line) (K). The CCI median cloud top was 780 m AGL and inversion base height was 865 m AGL [horizontal line in (a) and (b)]. (c) As in (a) and (b) but around the 1721 UTC 26 Aug 2008 radiosounding profile. The CII median cloud top was 1140 m AGL and the inversion-base height was 995 m AGL [horizontal line in (c) and (d)]. Vertical dashed line in (a) and (c) indicates the time of radiosounding release.

cloud base observed by the ceilometer at 610 m AGL; the temperature inversion base was observed at 865 m AGL. Cloud top for the CII case was 1140 m AGL with a base observed at 810 m, with a deeper layer of hydrometeors falling from the cloud layer. Here the inversion base was 995 m AGL, thus the cloud top extended approximately 140 m above the inversion.

The total fraction of profiles when a cloud top and temperature inversion are collocated according to these thresholds is given, black in Fig. 3a, relative to the total number of cloud-containing profiles for each location (number in brackets). The occurrence frequency of these cloud-inversion regimes is largest for ASCOS but still less than half of all profiles. For SHEBA and Barrow, the occurrences are even lower. These relatively low frequencies are significantly impacted by the regime definitions that require the cloud top to be more than 90 m above the inversion base, or the cloud to be no greater than the inversion base. A relaxation of the thresholds by one radar range gate (45 m) for both cloud-inversion

regime definitions increased the relative frequencies to 63%, 52%, and 45% over ASCOS, SHEBA, and Barrow, respectively. In addition, only temperature inversions at least 40 m thick are examined, and further inspection reveals that thinner inversions do exist in the vicinity of low clouds but are excluded from the statistics here. We choose stricter definitions, and hence a reduction in data coverage, to focus on clearly defined, robust cloud-inversion interaction cases to better understand the physics responsible for the regime separation and to bypass the potential analysis of a transition from one regime to the other.

Subdividing the cloud-inversion collocations by regime reveals the dominance of the CII regime at both sea-ice-based sites (Fig. 3a). Over ASCOS, CII occurred nearly three times as often as CCI, which is comparable to the frequency observed in Sedlar and Tjernström (2009). Over Barrow, the regimes are reversed and the CCI regime clearly dominates. Generally the CCI cases have cloud tops slightly larger than one radar range gate

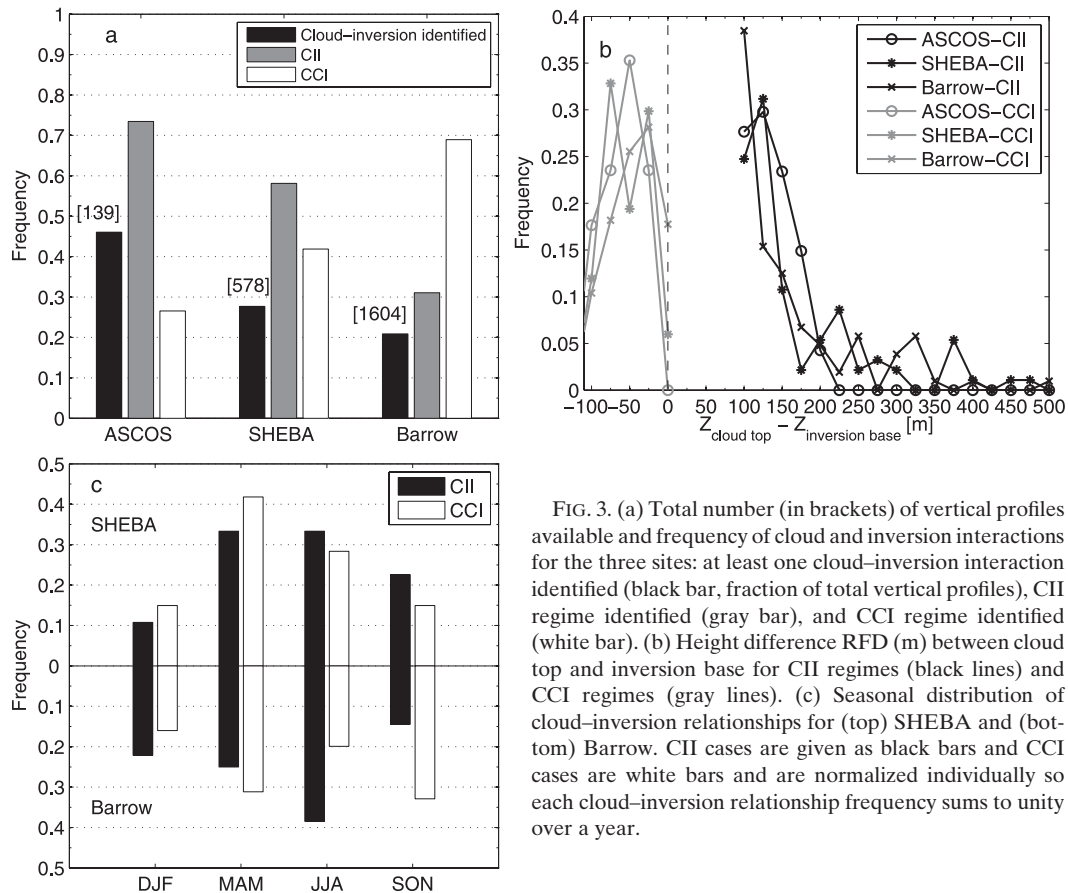


FIG. 3. (a) Total number (in brackets) of vertical profiles available and frequency of cloud and inversion interactions for the three sites: at least one cloud–inversion interaction identified (black bar, fraction of total vertical profiles), CII regime identified (gray bar), and CCI regime identified (white bar). (b) Height difference RFD (m) between cloud top and inversion base for CII regimes (black lines) and CCI regimes (gray lines). (c) Seasonal distribution of cloud–inversion relationships for (top) SHEBA and (bottom) Barrow. CII cases are given as black bars and CCI cases are white bars and are normalized individually so each cloud–inversion relationship frequency sums to unity over a year.

below the inversion base (Fig. 3b). The CII geometric differences commonly ranged from 90 to 150 m and more for the sea ice sites, and the thickness relative frequency distributions (RFDs) have long positive tails revealing an occasional deeper extension into the temperature inversion structure.

The majority of cloud–inversion collocations occur from spring through autumn (Fig. 3c) when cloud fraction over the Arctic generally increases (Curry et al. 1996; Wang and Key 2005; Shupe et al. 2011). The CII regime is most common from spring to summer over both SHEBA and Barrow. The CCI regime at SHEBA reaches a maximum occurrence during spring and declines throughout the subsequent seasons, while at Barrow relative maxima occur during both spring and autumn. There is an increase from autumn to winter in CII occurrence at Barrow not observed in either regime at SHEBA.

b. Cloud geometry

Cloud-top and cloud-base height RFDs are given for CII and CCI regimes at each location in Fig. 4. In general, cloud–inversion collocations are most common with the lowest clouds. Base heights are often below 600 m, closer

to 300 m for the sea ice sites, and were lowest with CII (Figs. 4d–f). Corresponding cloud-top heights were often below 1500 m (Figs. 4a–c). Above 2000 m, almost all collocations were of the CCI type. In terms of median values, CCI median cloud-top heights were 215, 315, and 450 m higher than tops for CII clouds over Barrow, ASCOS, and SHEBA, respectively.

c. Cloud LWP

Single- and multilayered cloud systems were observed at all sites and for both cloud–inversion regimes. Integrated liquid water path RFDs for only single-layer clouds indicate liquid water paths (LWPs) frequently ranging from 0 to 100 g m^{-2} (Fig. 5). Clouds begin emitting radiation as a blackbody between about 30 and 50 g m^{-2} (e.g., Stephens 1978). CII LWPs were slightly larger than those during CCI cases for both ASCOS and SHEBA, however relatively few single-layer cases bias the CCI statistics at ASCOS, causing the LWP distribution to fall primarily into three distinct bins. An analysis of cloud thickness (not shown) revealed no significant differences between the cloud regimes, suggesting that the CII regimes contained slightly more cloud

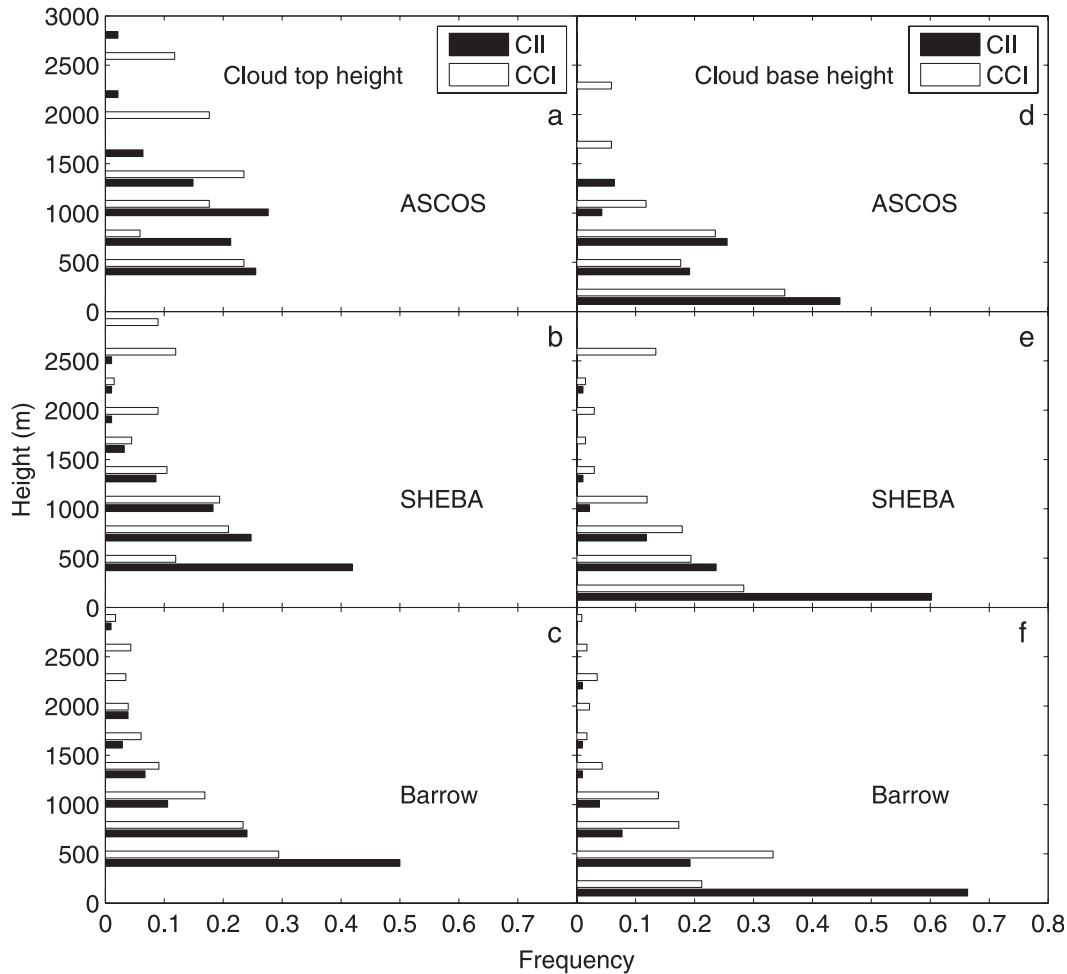


FIG. 4. Histograms of (a)–(c) cloud-top height and (d)–(f) cloud-base height (m AGL) for each observing site. CII (CCI) regimes are given as black (white) bars. Bin size is 300 m and centered in the interval.

liquid water than CCI for reasons other than geometrical thickness. Barrow's distinct peaks at 0 g m^{-2} suggest that the amount of liquid condensate varies with seasonal temperature changes. A LWP measurement of -25 g m^{-2} can safely be assumed liquid-free considering instrument uncertainty. Thus we cannot say with certainty that these single-layer clouds below 3000 m are liquid free.

4. Thermodynamic properties

a. Temperature inversions

Temperature inversion thicknesses, top minus base height, primarily range between 100 and 500 m (Figs. 6a–c). The thinnest inversions tend to be associated with CCI cases. The inversion strengths, top minus base temperature, are also weakest across inversions associated with the CCI cases (Figs. 6d–f), while larger strengths are more common for the CII cases. In general, inversion

strengths below 2 K were collocated with CCI cases. These results agree with those identified in Sedlar and Tjernström (2009), where deeper and stronger inversions were more often associated with the CII regime. The presence of cloud above inversion base appears to be uninhibited by increased static stability associated with inversion structures. These differences in regimes for collocated inversions tend to suggest that horizontal advection of heat is important for maintaining a stronger and deeper inversion for the CII cases in the presence of a cloud layer that is radiatively cooling to space. Both inversion thicknesses and strengths agree well with climatological observations within the Arctic (Kahl 1990; Serreze et al. 1992).

Comparison of inversion-base temperatures across observing sites is difficult, reflecting the impacts of the seasonal cycle (Figs. 6g–i). Temperatures during late-summer ASCOS range mainly from -10° to $+5^\circ\text{C}$ and are more often cooler during the CII regime. Inversion-base

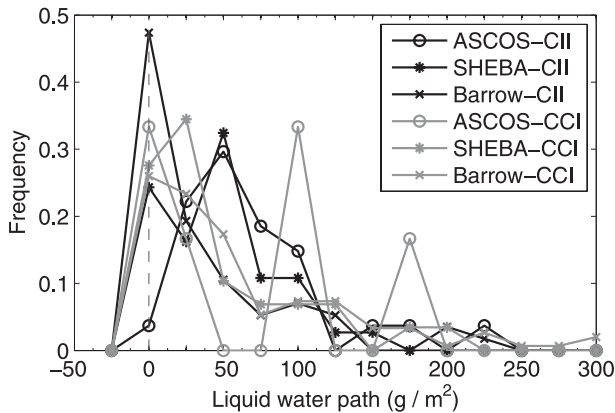


FIG. 5. Frequency of single-layer integrated cloud LWP (g m^{-2}); 0 g m^{-2} LWPs are shown considering the 25 g m^{-2} instrument uncertainty. CII (CCI) regimes are in black (gray).

temperature RFDs for SHEBA are very similar for the two regimes. At Barrow, CII inversion-base temperatures often are $\pm 2.5^\circ\text{C}$ or below -25°C ; CCI temperatures are, instead, generally between these RFD peaks.

Following the imposed regime definitions, CCI cloud-top temperatures should be similar to the inversion-base temperatures, and the distributions do agree quite closely (Figs. 6j–l). CII cloud-top temperatures, however, are warmer than the inversion base and depend on the inversion strength and cloud extension into the inversion. At least one mode in all cloud-top temperature RFDs is above -10°C , suggesting increased potential for supercooled cloud droplets (e.g., Pruppacher and Klett 1997). The colder clouds over SHEBA and Barrow suggest an increasing ice-to-liquid ratio (Shupe et al. 2006), although supercooled liquid has been identified down to temperatures below -34°C (Intrieri et al. 2002b).

b. Thermodynamic stability

Subcloud and cloud-layer static stability are analyzed here to examine the potential vertical mixing characteristics. Equivalent potential temperature vertical gradients were computed from the surface to the inversion base. Statistics are shown as box-and-whisker plots in Fig. 7 (see caption). Gradients above or below zero indicate static stability and potential instability, respectively, while those near zero represent neutral static stability. For comparison, heights are normalized by the surface ($z_n = 0$), cloud-base ($z_n = 0.5$), and inversion-base ($z_n = 1$) heights. Black boxes indicate when the median CII and CCI gradients at a normalized level are significantly different at the 95% confidence level.

In general, the largest potential static instability is observed nearest the surface. The significant seasonal variation in near-surface stability at Barrow is apparent, although the near-surface gradients at SHEBA lack the

spread toward large positive values. Strong static stability emerges near the inversion base ($z_n = 1$), suggesting the occurrence of cloud-top entrainment of relatively warmer air from above the inversion base downward into the cloud layer.

Equivalent potential temperature gradients were potentially unstable or neutral up to $z_n = 0.2$ for CII regimes at all locations. Between $z_n = 0.2$ and 0.4 , approximately, increased static stability emerged and either remained up to cloud base (Figs. 7b,c) or trended slightly back to near-neutral stability (Figs. 7a,d,e). These characteristics indicate a general statically stable layer overriding a shallow, near-surface layer with reduced static stability. Such a feature would act to limit the coupling statically between the cloud base and subcloud layer. The slight recovery to near-neutral values below cloud base reflects cloud-driven circulations extending into the subcloud layer; this occurred mainly for CII regimes over ASCOS and Barrow and for the CCI regime over SHEBA. Harrington et al. (1999) find that subcloud stability can develop through ice crystal sublimation and water vapor loading as crystals fall into a subsaturated layer. Such a mechanism is possible, as mixed-phase clouds with falling ice crystals were common during the ASCOS (Sedlar et al. 2011) and SHEBA (Intrieri et al. 2002b; Shupe and Intrieri 2004; Shupe et al. 2006) ice drifts and at Barrow (Shupe et al. 2006; Shupe 2011), but these crystals did not always reach the surface (Shupe and Intrieri 2004; Sedlar et al. 2011). The entire subcloud layer is neutral or well-mixed at Barrow for the CCI regime, indicating a coupling between the surface and cloud layer. This coupling may be achieved by cloud-generated buoyancy, surface heating, or through cool-air advection from the Arctic Ocean (Curry et al. 1997). Barrow was the only site where median subcloud equivalent potential temperature gradients between CII and CCI regimes were significantly different.

In-cloud ($z_n = 0.5$ – 1) gradients for both regimes at SHEBA and Barrow are stable, albeit slightly more neutral for the CCI regime at the latter site. Median in-cloud gradients over ASCOS are primarily unstable or neutral for CII cases, while more stable within CCI cases. There is a lack of significantly different in-cloud median gradients across regimes for ASCOS and SHEBA. However, if we examine the bulk cloud layer, $z_n = 0.50$ – 0.85 , the median in-cloud gradient is less stable for the CII regime and is statistically significantly different at the 95% confidence level compared to the CCI regime over both ASCOS and SHEBA. Thus, cloud-scale vertical mixing may be a potential mechanism allowing an overshooting of the cloud above the temperature inversion base, as speculated in Sedlar and Tjernström (2009). This vertical mixing, once below

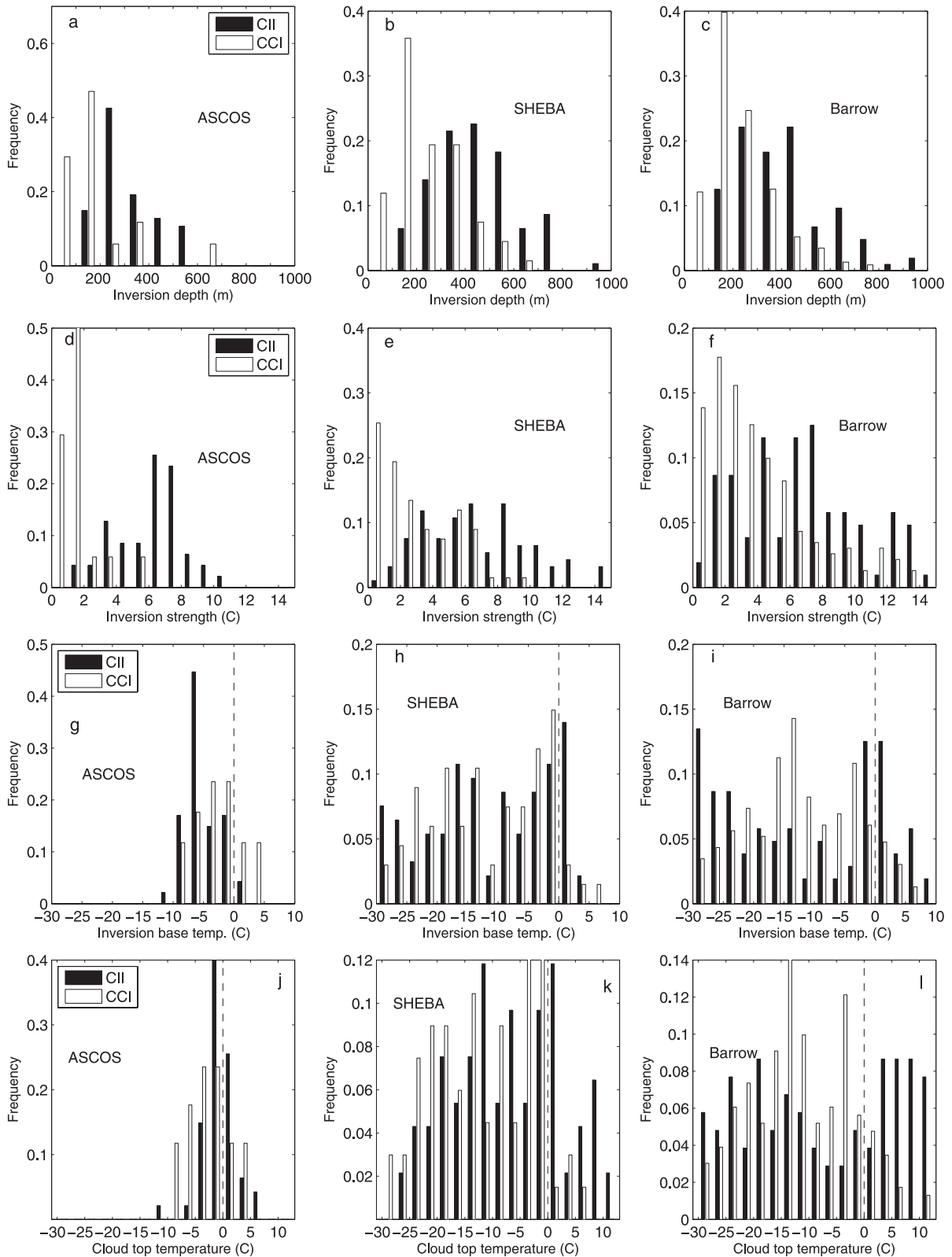


FIG. 6. Histograms of temperature inversion properties characterizing CII (black bars) and CCI (white bars) regimes for each observing site: (a)–(c) inversion depth (top minus base height, 100-m bins), (d)–(f) inversion strength (top minus base temperature, 1°C bins), (g)–(i) inversion-base temperature (2.5°C bins), and (j)–(l) cloud-top temperature (2.5°C bins).

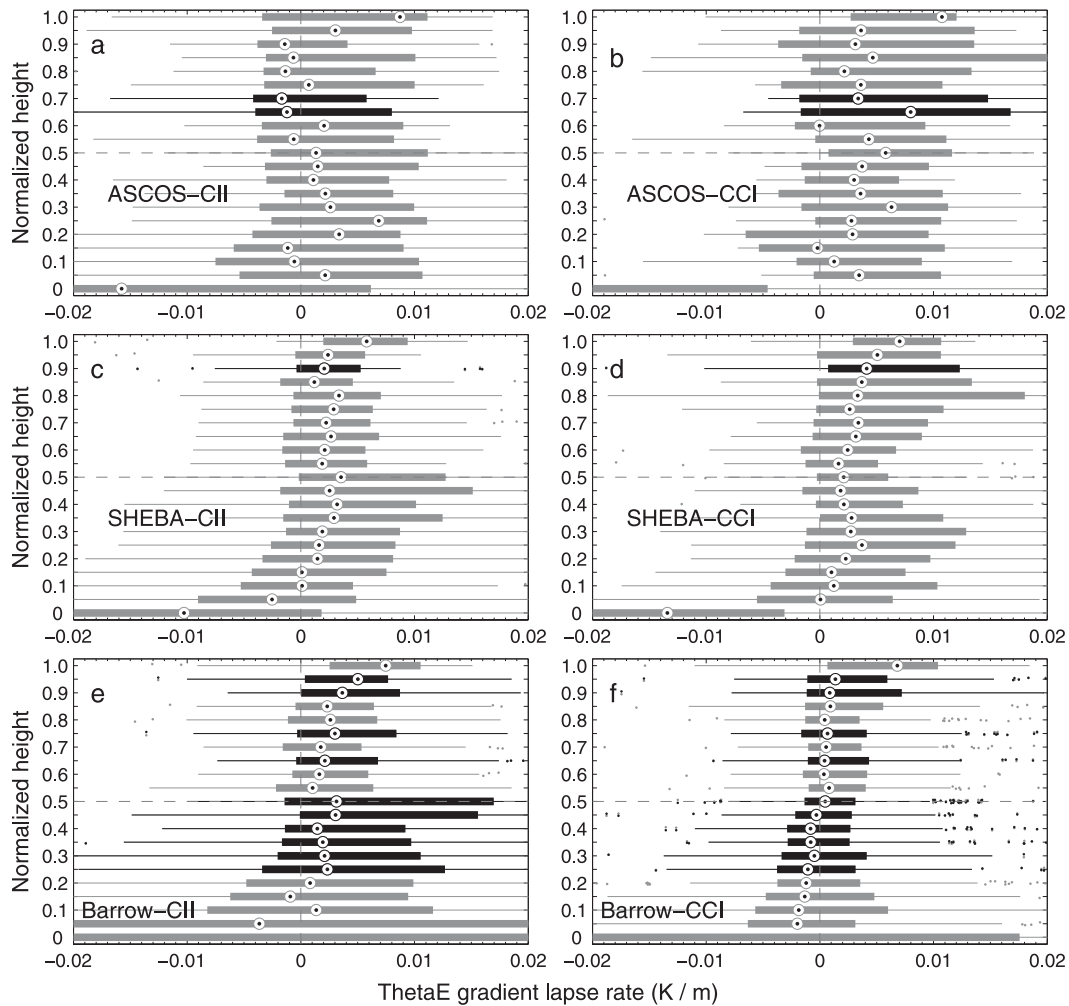


FIG. 7. Box-and-whisker plots of gradient equivalent potential temperature lapse rates (K m^{-1}) computed from radiosoundings for (a),(b) ASCOS, (c),(d) SHEBA, and (e),(f) Barrow; lapse rates for (left) CII regimes and (right) CCI regimes. Heights are normalized (z_n) such that $z_n = 0$ represents the surface, $z_n = 0.5$ is cloud-base height, and $z_n = 1$ is inversion-base height. Median values are indicated by the circle within the box, edges of the box mark the lower and upper quartiles, whiskers (thin solid lines) represent extent of data that is 1.5 times the difference between upper and lower quartiles, and the outliers (small circles) are data points outside of the whisker range. Black box-and-whisker levels denote median values that are statistically significantly different between regimes. Note the full extent of lapse rates observed is not shown to place focus on the majority of data points.

cloud base, however, is not coupled with the surface and suggests that horizontal advection of heat and moisture versus vertical mixing from the surface may be the primary mechanism sustaining cloud formation.

c. Temperature inversion slope

The slope of the temperature increase from inversion base to top is used as a proxy for static stability inside the inversion and also as a measure of the cloud impacts on the thermodynamic profile. In Fig. 8, normalized temperature and normalized height over the inversion structure are shown as RFD contours. Normalized temperatures following the 1:1 line have a constant increase

with height. Such an increase is observed for CCI regimes over ASCOS and sometimes at SHEBA (Figs. 8d,e). The linear temperature slope associated with these CCI cases, however, may be smoothed by cloud-generated motions, which we have no means to quantify. For instance, strong cloud-top cooling causing intense localized downdrafts may yield increased potential entrainment of warmer air from above the inversion base that is replaced by slightly cooler detrained air.

The CII regimes over all sites (Figs. 8a–c) have a concave profile shape with strongest temperature increases above inversion base to $z_n = 0.3$ and generally weaker temperature increases above $z_n = 0.4$. Considering that

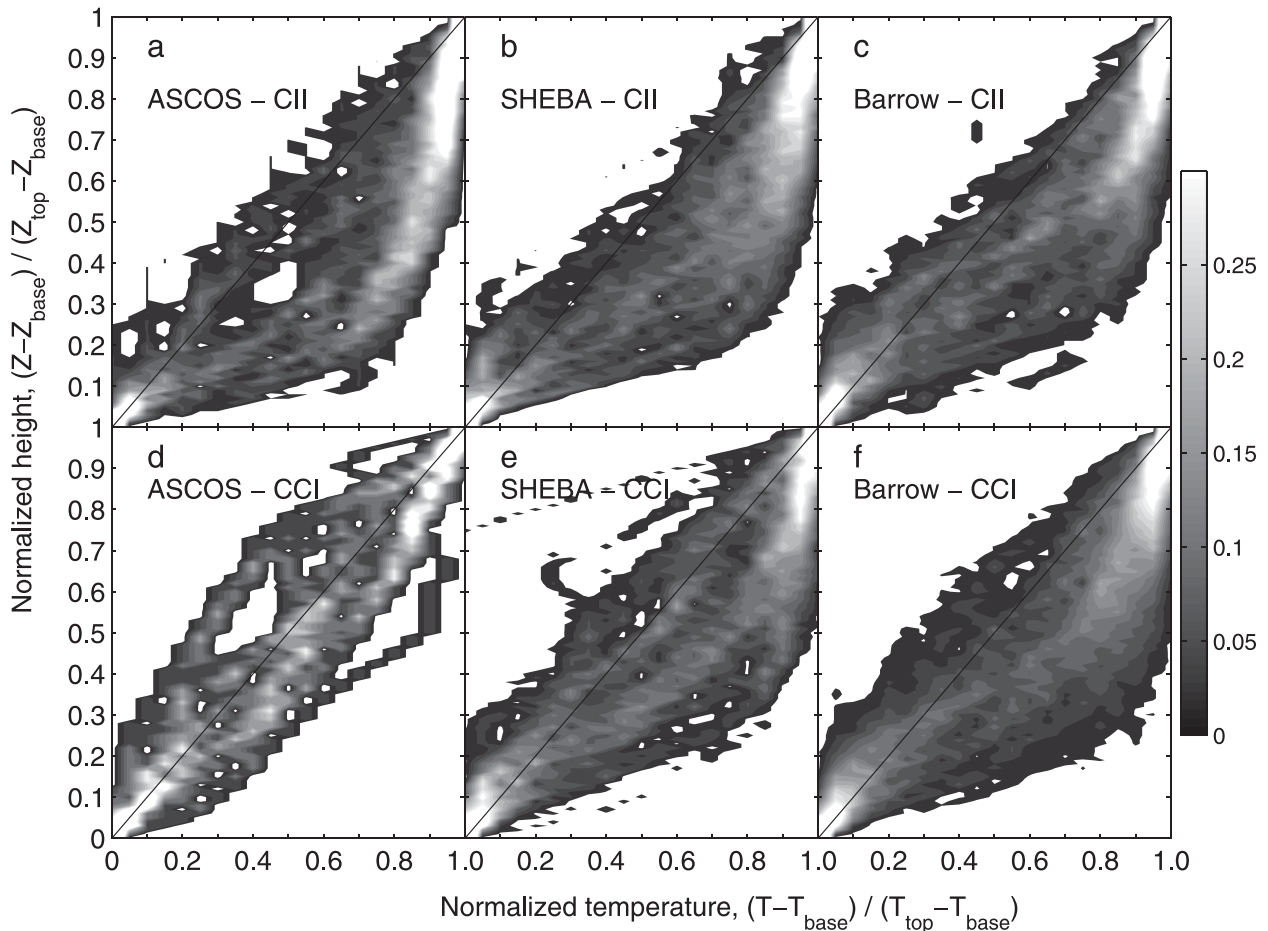


FIG. 8. RFDs (grayscale) of height across the temperature inversion normalized by the inversion depth vs the temperature increase normalized by the inversion strength for (a)–(c) CII regimes and (d)–(f) CCI regimes. The 1:1 line represents a constant increase of temperature with height over the inversion structure.

CII clouds are present where the strongest temperature increases are observed, an increase in specific moisture across the inversion base is thus also required following the Clausius–Clapeyron relation. The shape of the increasing temperature profiles also suggests that horizontal heat and moisture advection is important for maintaining the inversion structures when the cloud top extends above the inversion base. The concave slope pattern for CII regimes may occur if cloud longwave cooling continues to be largest near the inversion base and somewhat less in an optically thin portion of the cloud layer above the inversion base. Concave slope profiles are found for both cloud regimes over Barrow and often at SHEBA and cannot be explained by these mechanisms.

d. Specific humidity inversions

Often coinciding with Arctic temperature inversions are moisture inversions (Curry 1983; Curry et al. 1996; Tjernström et al. 2004). Figures 9a–c indicate that

moisture inversions occurred for 86%–94% of temperature inversions collocated with the CII regime. Moisture inversions also occurred during CCI regimes, although less frequently. Thus, the identification of a moisture inversion alone cannot explain the extent of cloud tops at or above the temperature inversion base.

The magnitude of absolute specific humidity increase is, in general, larger for the CII regimes (Figs. 9a–c). RFDs of the moisture-inversion depth, the distance above inversion-base height where specific humidity no longer increases with height, normalized by the depth of the temperature inversion are shown in Figs. 9d–f. Not all moisture inversions span the entire depth of the temperature inversion, and some are confined to a small fraction of the temperature inversion depth. Moisture inversions were not observed to be deeper than the temperature inversions. Moisture inversions associated with CII cases are generally thinner than those for CCI cases. However, these thinner but stronger moisture

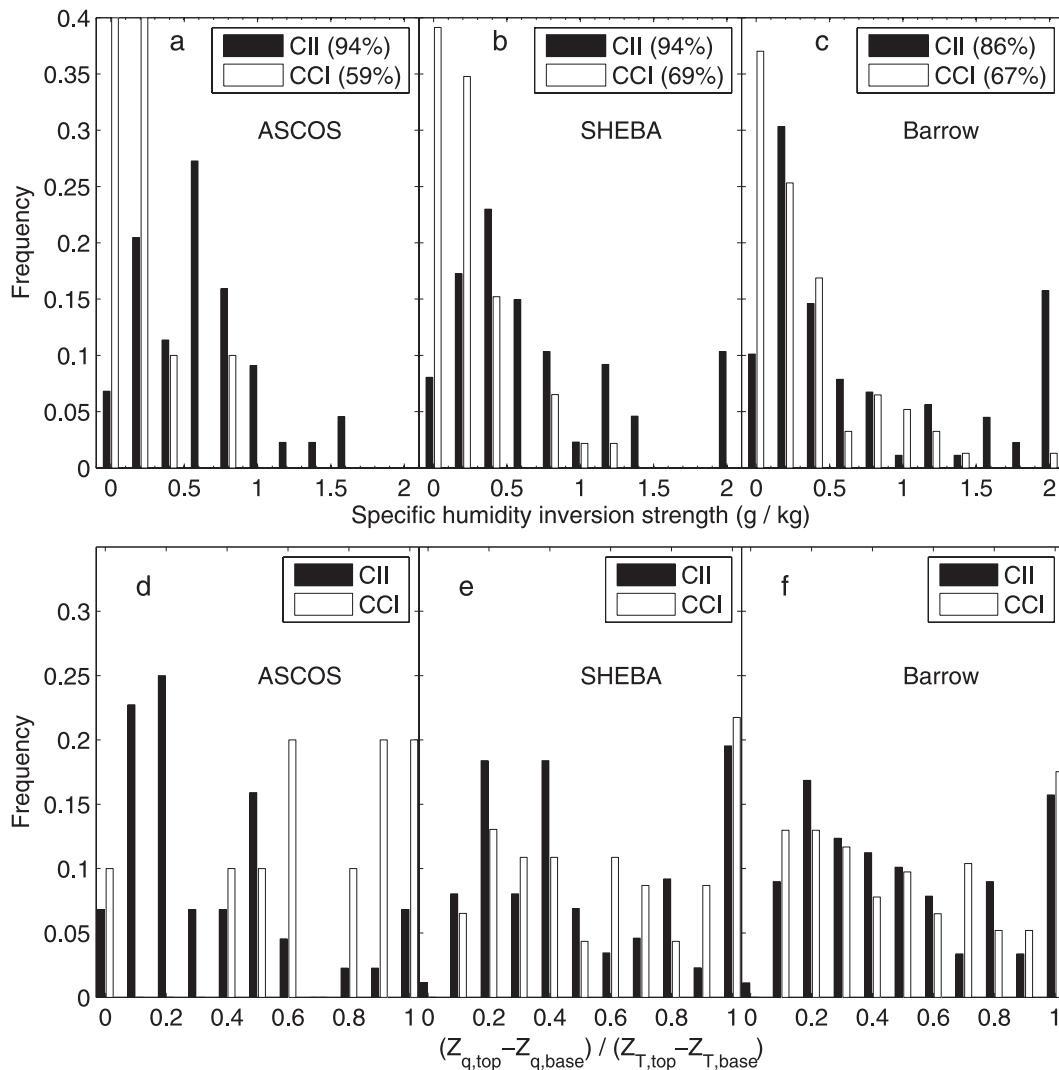


FIG. 9. (a)–(c) Moisture inversion coinciding with the temperature-inversion percentage occurrence (percentage in legend) and strength and (d)–(f) normalized moisture-inversion depth over temperature-inversion depth for CII (black bars) and CCI (white bars) regimes.

inversions match the location of strongest temperature increases above inversion base (Fig. 8).

The presence of a moisture inversion can have important implications for cloud growth and persistence. Turbulent motions or other dynamic instabilities near cloud top can result in entrainment that actually moistens the cloud layer (Solomon et al. 2011). This process might lead to additional condensation that helps maintain the cloud layer.

5. Cloud microstructure

Radars moments

The millimeter cloud radar (MMCR) moments are exploited statistically as proxies for some of the microphysical

and turbulent properties of these clouds. Shupe et al. (2006, 2008a) describe the use of MMCR moments for characterizing cloud phase, precipitation, and turbulence within a sample volume. The MMCR is designed to minimize the effects of wind shear and turbulent fluctuations on Doppler-determined velocities, thus the moments are typically dominated by effects of the cloud microphysical size distribution (Shupe et al. 2008b). All MMCR moments for 10 min following the radiosounding launch are interpolated to a normalized height grid similar to that in Fig. 7, where $z_n = 0$ is the surface, $z_n = 0.5$ is cloud base, and $z_n = 1$ is the inversion base. Heights above the inversion base are not interpolated; here each 0.01 height interval represents a 45-m radar range gate (see Fig. 10a).

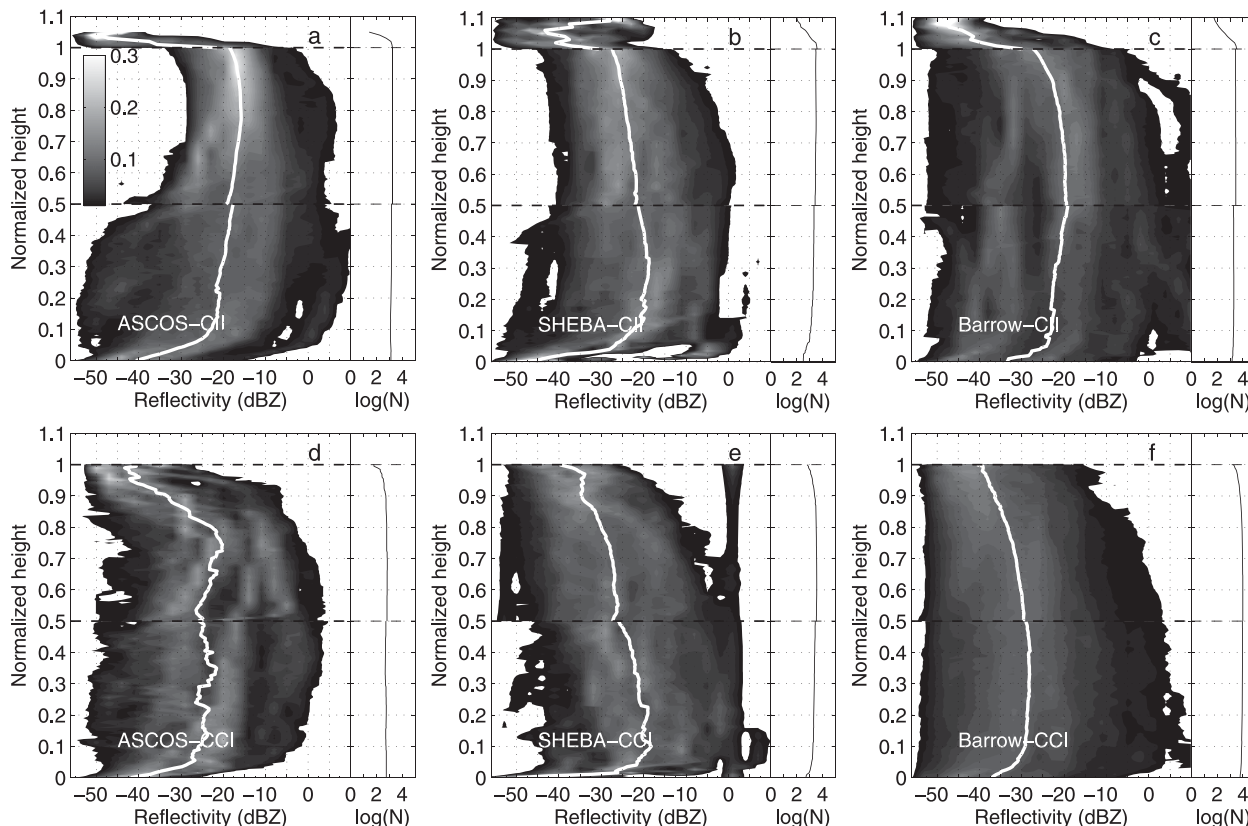


FIG. 10. Profile RFD contours of reflectivity (dBZ) for (a)–(c) CII regimes and (d)–(f) CCI regimes for each respective observation site [grayscale bar in (a) valid for (b)–(f)]. The white profile line is the median. Heights are normalized as in Fig. 7, where $z_n = 0$ is the surface, $z_n = 0.5$ is cloud base height, and $z_n = 1$ is inversion base height. Heights above $z_n = 1$ represent the cloud layer above the inversion base and are not normalized. Here every 0.01 height increment corresponds to one 45-m MMCR range gate. The profile of the logarithm of the number of observations (N) at each height is included (far right in each panel).

Radar reflectivity RFDs and median profiles are shown in Fig. 10. Radar reflectivity is backscattered power (dBZ) sensitive to the size of the scattering hydrometeors to the sixth power. A typical upper bound for reflectivities from a volume containing only cloud droplets is about -17 dBZ (Frisch et al. 1995). In-cloud reflectivity for the CII cases tends to decrease slightly with height at all sites, apart from a slight increase with height at lower in-cloud heights at ASCOS. For CCI (Figs. 10d–f) there is a more pronounced decrease with height except for an increase at lower in-cloud heights at ASCOS. Below cloud base, where only solid or liquid precipitation occurs, reflectivity only slightly increases or decreases before more sharply decreasing near the surface as precipitation evaporates/sublimates.

Median values at inversion base range from -45 to -40 dBZ for CCI regimes, while the range was generally -27 to -17 dBZ for CII regimes. For the CII cases, reflectivity above the inversion base decreases significantly with height, approaching CCI cloud-top minimum

values or less. These small backscatter magnitudes near cloud top likely represent small, liquid droplets without precipitation-size particles; increasing reflectivity at cloud top for SHEBA CII is associated with only two events, reflected in the reduced number of observations at that height. The general reflectivity increase from cloud top to base reflects the development and growth of ice or liquid precipitation hydrometeors, which are larger than the cloud droplets and thus have a larger backscatter (Shupe et al. 2004). Interestingly, the RFDs near inversion base indicate typically larger reflectivities for the CII cases. A chi-squared distribution test reveals that the positive tails of the distributions greater than -10 dBZ and heights above 0.8 in Fig. 10 were significantly greater at the 99% level for CII cases compared to CCI cases. This may be an indication of increased hydrometeor sizes due to freezing and growth of ice crystals from a predominately liquid layer that lies above the coldest portion of the cloud.

Mean Doppler velocity (Fig. 11) is a measure of the mean vertical motion (m s^{-1}) of the hydrometeors

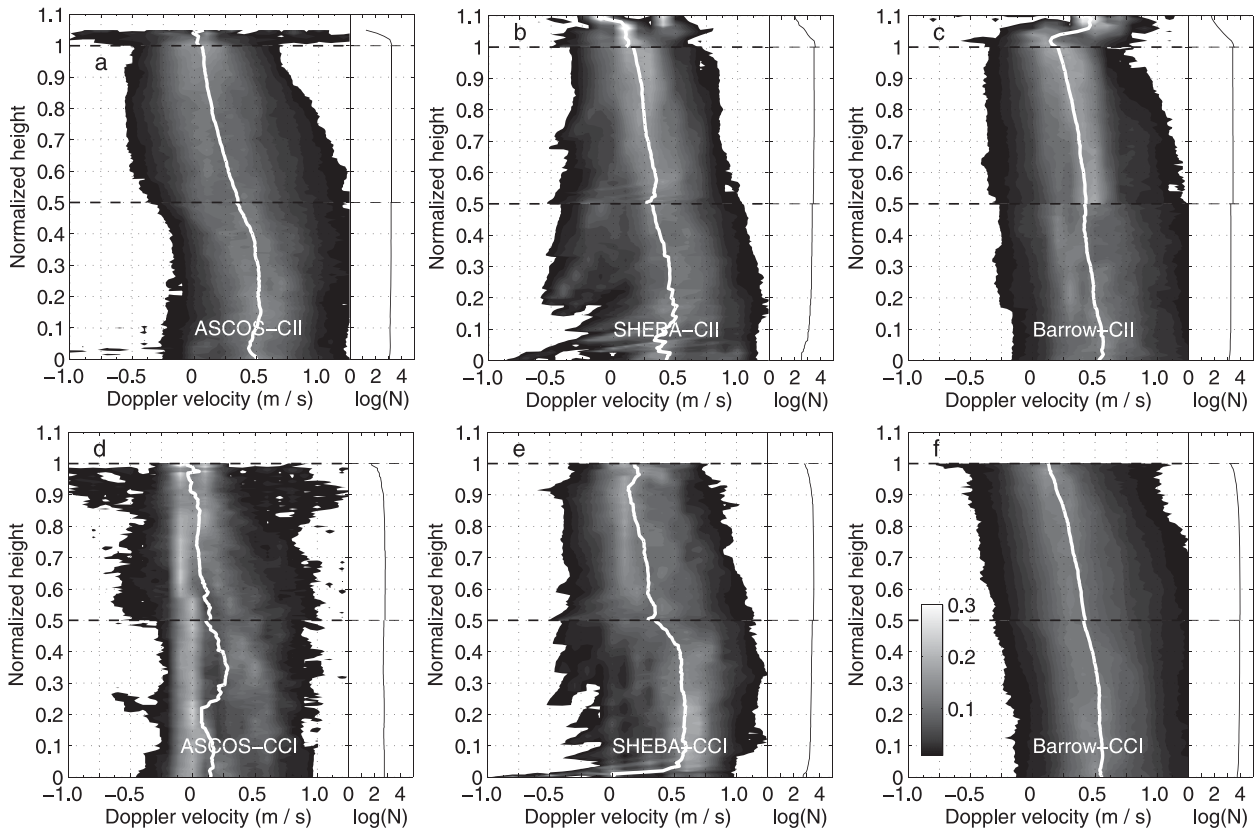


FIG. 11. As in Fig. 10 but for mean Doppler velocity (m s^{-1}).

in a radar pulse volume relative to the MMCR: here positive is falling. Cloud droplets, owing to their smaller size, generally have lower fall velocities compared to ice crystals, and may even move with vertical air motions. Except for CCI cases over ASCOS, median values are always positive, indicating a general falling motion. Magnitudes increase downward from cloud top to base and continue to increase through the subcloud layer. These are typical signatures of increasing hydrometeor size via growth through collisions and diffusion, with larger hydrometeors falling from the cloud. There is little difference between cloud-regime fall velocities at Barrow (Figs. 11c,f). Over ASCOS, the mean Doppler velocities are larger both in-cloud and below cloud base during CII cases. At SHEBA, the in-cloud velocities are comparable but Doppler velocities are larger in the subcloud layer during CCI cases. We identify the vertically resolved occurrences of reflectivity larger than -10 dBZ and Doppler velocity above zero as a simplistic metric for precipitation. Generally the vertical frequency of occurrence using this precipitation metric ranged between 10% and 30% of all cases, tending to be largest in the vicinity of cloud base. Based on regimes, we find

that, vertically, the CII cases passed the precipitation thresholds between 5% and 10% more frequently than the CCI cases, a significant result at the 99% confidence level using a chi-squared distribution test (not shown).

Near inversion base, median velocities generally decrease with height and are more frequently negative. Above inversion base, small near-zero velocities are common, although the absolute velocity range increases once again for ASCOS and, to some degree, for Barrow. The hydrometeors are likely small and are moving with variable air parcel motion. Positive velocities at the CII top over Barrow are unlikely to be influenced by larger droplets or ice crystals, like the statistics suggest, since nearly all reflectivities at cloud top were below -40 dBZ.

The Doppler spectrum width is the square root of the Doppler velocity variance within a sampling volume. A larger spectrum width indicates a broader velocity spectrum. The spectrum width RFDs suggest a general increase from inversion base downward to cloud base (Fig. 12). Such behavior indicates a convolution of velocity contributions from liquid droplets, drizzle-sized droplets, and/or ice crystals at a wide range of sizes.

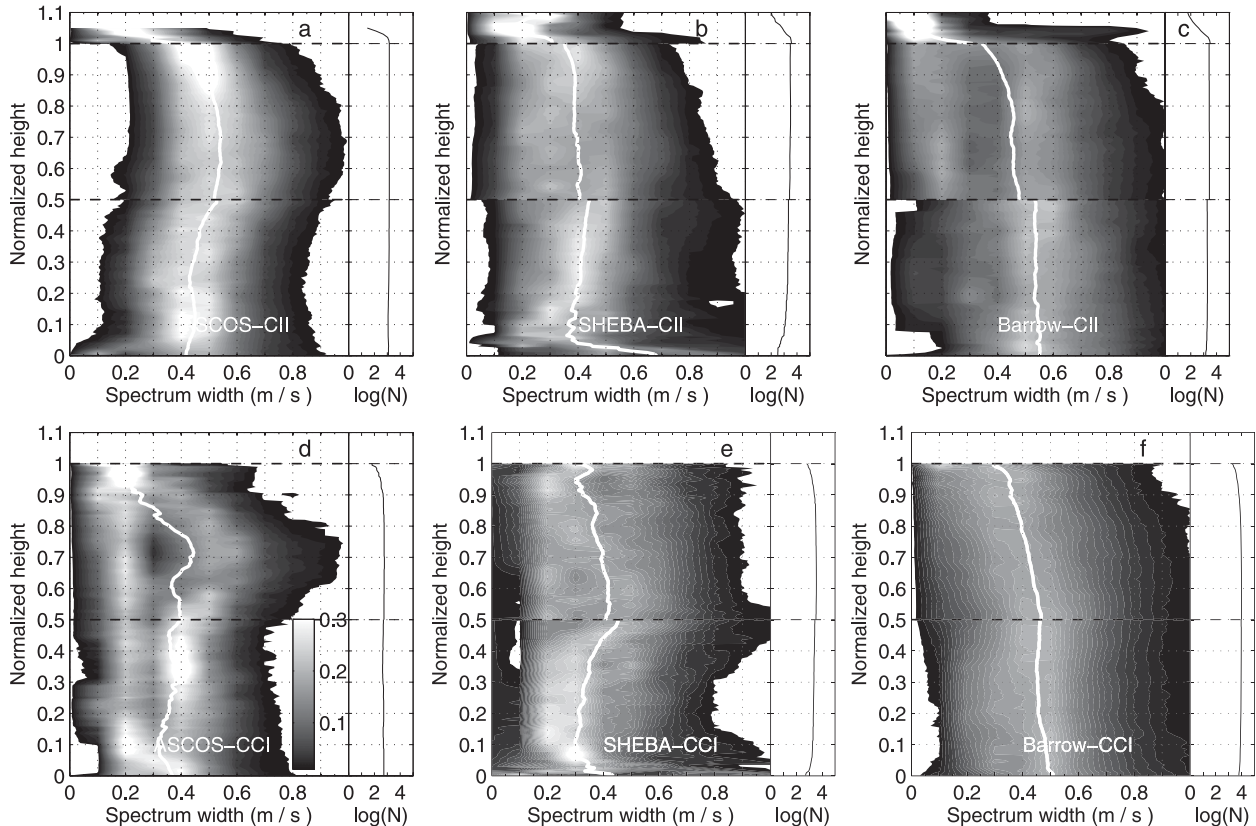


FIG. 12. As in Fig. 10 but for spectrum width (m s^{-1}).

Below cloud base the spectrum width decreases or remains constant with decreasing height except for an increase right near the surface in some cases that may be associated with surface turbulence.

Spectrum width values decrease rapidly above inversion base (Figs. 12a–c). The reduction in variance, coupled with generally small vertical velocities and reflectivities, indicates that this portion of the cloud is likely composed of small liquid droplets (Zuidema et al. 2005; Shupe et al. 2006, 2008a; Sedlar and Tjernström 2009) moving with the air motions. Sedlar and Tjernström (2009) found evidence for two unique cloud layer compositions above inversions: one that suggested only liquid droplets and a second that was dominated by ice-phase hydrometeors above the inversion. Here we find no evidence of ice above the inversion. Within the cloud layer we do find a clear mixed-phase cloud signature, as did Sedlar and Tjernström (2009), with reflectivities higher than those expected for liquid droplets (i.e., indicative, instead, of larger ice crystals) occurring above cloud base. All CCI radar moments show similar decreases near cloud top, suggesting that liquid droplets also dominate the upper portions of the cloud layer for this regime.

6. Longwave forcing effect

The presence of cloud liquid above the temperature inversion has interesting implications for the radiative transfer for this cloud regime. Longwave radiative absorption and transmission through a cloud layer are functions of cloud longwave optical depth, cloud phase, and particle size, and emitting temperature (e.g., Stephens 1978). Longwave flux follows the Stefan–Boltzmann relationship,

$$F = \varepsilon \sigma T^4, \quad (1)$$

where F is the flux, ε is the apparent emissivity, σ ($5.67 \times 10^{-8} \text{ W m}^{-2} \text{ K}^{-4}$) is the Stefan–Boltzmann constant, and $T(\text{K})$ is the emitting (blackbody) temperature. Cloud longwave emissivity is a function of the longwave optical depth and has often been specified as a function of LWP with the following form:

$$\varepsilon = 1 - \exp[-a_0 \text{LWP}], \quad (2)$$

where a_0 ($\text{m}^2 \text{ g}^{-1}$) is the mass-absorption coefficient (Stephens 1978). Emissivity approaches unity as LWP increases, often fully opaque when LWP ranges between

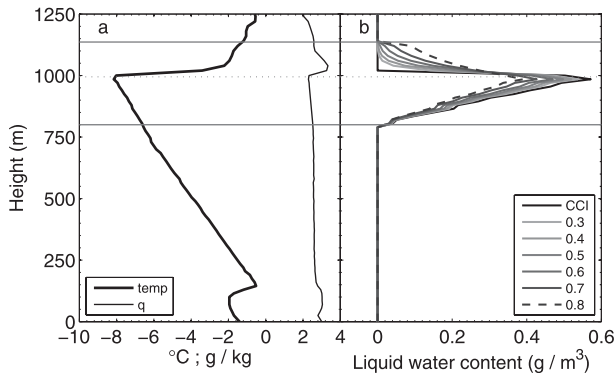


FIG. 13. (a) Temperature (thick line, $^{\circ}\text{C}$) and specific humidity (thin line, g kg^{-1}) from a radiosounding profile during the ASCOS drift and (b) LWC profiles (g m^{-3}) calculated using the observed cloud boundaries and thermodynamic profile, constrained by the observed cloud LWP. The lines represent varying LWC distributions by changing the multiplication factor of LWC retained from the previous vertical level within the temperature inversion. The larger the factor, the more total liquid water is displaced above the temperature inversion base. CCI represents a cloud capped by the inversion base (same as a multiplication factor of 0).

30 and 50 g m^{-2} (Stephens 1978; Shupe and Intrieri 2004; Sedlar et al. 2011). Particle size, shown to alter cloud apparent emissivity by as much as 8% for nonopaque clouds (Garrett et al. 2002; Garrett and Zhao 2006), is not explicitly included in Eq. (2). A cloud layer with liquid water above the inversion will have a different emissivity and emitting temperature relative to a cloud with liquid water extending only to the inversion base height. Thus, a change in the emitted longwave flux based on Eqs. (1) and (2) is expected. We examine these impacts of cloud liquid redistribution in terms of a longwave radiative forcing for the CII regime relative to the CCI regime. Shortwave radiative forcing via liquid redistribution is absent or minimal, and thus ignored, since we assume the same total LWP and droplet size for both cloudy cases.

a. Method

We use the Rapid Radiative Transfer Model (RRTM) (Mlawer et al. 1997) to examine the cloud-longwave radiative interaction by computing broadband longwave flux and cooling rate profiles. Model inputs include a reference latitude, thermodynamic profiles, surface skin temperature and emissivity (unity), a carbon dioxide mixing ratio, cloud boundaries, a cloud liquid water content (LWC) profile, and a cloud-droplet effective radius profile. Sensitivity calculations have been made holding cloud LWP constant while varying the ice/water path within the cloud layer within reason, but the flux differences compared to liquid-only clouds were negligible as the total cloud optical depth is typically dominated by liquid droplets. Therefore we consider liquid-only

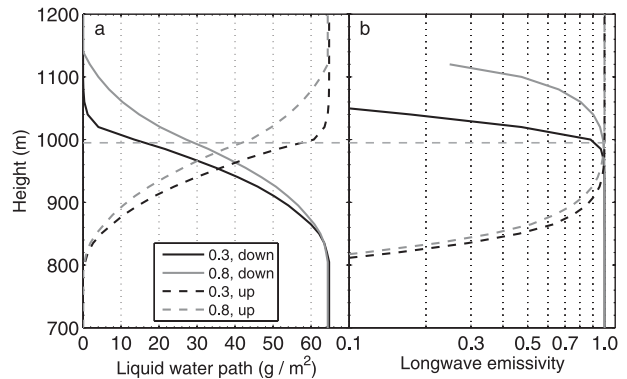


FIG. 14. (a) LWP (g m^{-2}) as a function of height (m) integrated for both a top-down (solid lines) and bottom-up (dashed lines) approach for two distributions of LWC: 0.3 (30%) retained from previous vertical level (black lines) and 0.8 (80%) retained from previous vertical level (gray lines). (b) Effective emissivity calculated using the integrated LWP and Eq. (2). The mass absorption coefficient is a constant broadband value of 0.158 for downward radiation and 0.13 for upward radiation (Stephens 1978). Thermodynamic and cloud boundaries are the same as in Figs. 2c,d, 13. The gray dashed horizontal line represents the inversion-base height.

clouds in the following discussion. We assume a constant droplet effective radius of $8 \mu\text{m}$, typical for Arctic low-level stratiform clouds (Curry et al. 1996; Shupe et al. 2001).

A single-layer cloudy case from 26 August 2008 during ASCOS is used to examine the longwave impact with cloud liquid water within the inversion (same case as in Figs. 2c,d). For this case, the ceilometer-observed cloud base was near 810 m AGL and the inversion base was at 995 m AGL (Fig. 13a). The inversion depth and strength were approximately 250 m and 8°C , and the temperature increases above the inversion behave like the concave profiles typical of CII cases during ASCOS. The observed cloud layer extended 145 m above the inversion base with a top at 1140 m AGL. This stratiform cloud layer persisted for approximately 5 days, with slightly varying cloud geometry, LWC, and presence of ice crystal precipitation (cf. Sedlar et al. 2011). The observed LWP at the time of the thermodynamic profile was 65 g m^{-2} .

b. LWC profiles

Adiabatic LWC profiles are calculated using the observed thermodynamic profile and cloud boundaries. However, within temperature inversions, adiabatic LWC calculations cannot be made. We circumvent this drawback by multiplying the final LWC approximation at inversion base by a constant decimal factor. We continue to multiply the respective residual LWC estimate by the constant to obtain a value for the next vertical layer.

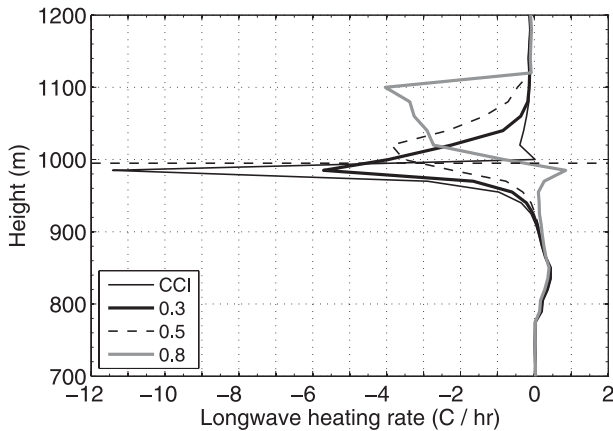


FIG. 15. Longwave heating rates ($^{\circ}\text{C h}^{-1}$) as a function of height (m) for a cloud containing 65 g m^{-2} LWP and a droplet effective radius of $8 \mu\text{m}$; thermodynamics and cloud boundaries as in Figs. 2c,d, 13. The distribution of LWC is shown for a cloud whose top is forced at the inversion base (CCI) and three different displacements of LWC above the inversion base; higher factor means more LWC retained within the temperature inversion. The dashed horizontal line represents the inversion base height.

Therefore, we have a continually diminishing LWC profile from inversion base to top where LWC is then set to zero. We use a range of multiplication factors from 0 to 0.9, effectively altering the total amount of cloud liquid displaced above the inversion base. The estimated LWC profiles are then integrated and scaled by a common cloud LWP, ensuring that the total cloud liquid is the same for longwave intercomparisons of different profiles.

Examples of hypothetical LWC profiles are shown in Fig. 13b. CCI represents a LWC profile with cloud top bounded vertically by the inversion base. The larger the decimal factor, the more liquid water is retained from the previous lower vertical level; thus a larger fraction of the total cloud water resides above the inversion base. The percentages of total LWP displaced above the inversion base range from 17% for the factor 0.1 to 49% for factor 0.9. We first examine the impacts on longwave radiation using the total LWP observed at the time of the case (65 g m^{-2}). Then we perform longwave sensitivity tests by keeping the cloud boundaries the same but reducing the total cloud LWP.

c. Longwave impacts resulting from LWC redistributions

The vertically cumulative LWP and longwave emissivity profiles for two example LWC distributions are shown in Fig. 14. For the factor 0.3, 21% of total LWP is redistributed above the inversion base while for the 0.8 factor it is twice as much—42% of total LWP is redistributed. The effective emissivity (Fig. 14b) clearly increases exponentially with LWP. For the top-down

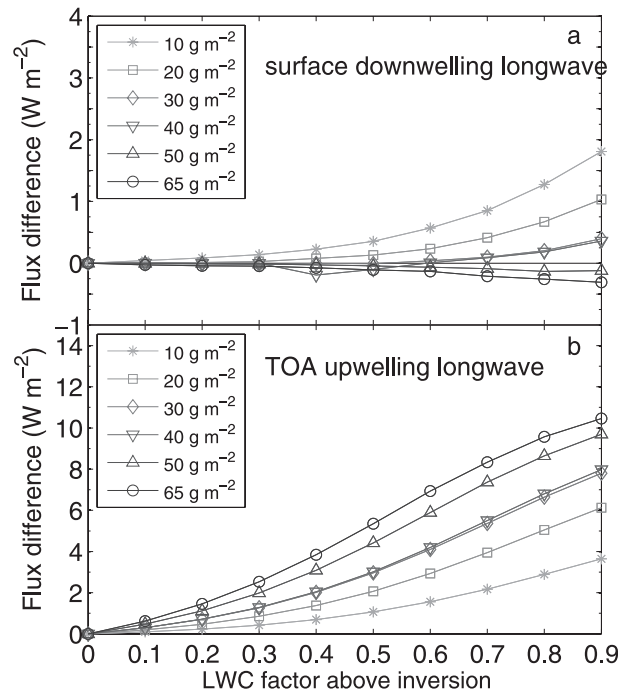


FIG. 16. Modeled longwave radiative flux difference (W m^{-2}) at the (a) surface and (b) TOA as a function of the amount of LWC displaced within the temperature inversion (fraction retained from previous vertical level: higher factor represents more LWC within the inversion). Flux difference is defined as the longwave radiative flux from a cloud with a percentage of LWC retained above inversion base minus that of a cloud with same total LWP but whose top is forced to remain at the inversion base (the CCI regime; multiplication factor of 0). The lines represent sensitivity tests by varying the total cloud LWP; LWP of 65 g m^{-2} was the observed value at the time of the thermodynamic profile in Figs. 2c,d, 13.

integration, the emissivity for the 0.8 LWC profile approaches unity at a higher altitude compared to the 0.3 profile with less water above the inversion. The cloud emission temperature is also larger since more liquid water is located at a warmer temperature above the inversion base. However, we see that with the bottom-up integration, the cloud layer below the inversion base is already opaque to longwave radiation. Thus, the enhanced longwave flux from the liquid within the inversion is absorbed within the cloud layer itself. On the other hand, the cloud with a 0.3 LWC profile becomes opaque closer to the cloud base since less of the total cloud LWC is redistributed within the inversion. Any enhanced flux from above the inversion is masked by the cloud layer emitting radiation to the surface from a lower, and therefore warmer, effective altitude.

Figure 15 demonstrates that, as longwave optical depth above the inversion increases, shallow layers of intense longwave cooling from cloud top decrease, in this case up to threefold relative to a typical adiabatic CCI cloud.

However, the cooling is permitted over a greater cloud depth due to the change in cloud opacity. Reductions in peak cooling rates relative to that from the CCI profile suggest that cloud-top cooling is not the reason for the stronger temperature inversions observed during CII cases. However, longwave absorption by droplets within the inversion may impact the thermodynamic structure causing sharp warming over a shallow layer. A flux convergence below the inversion base causes a positive heating rate for the 0.8 LWC profile. This local heating will act to stabilize the cloud layer to ascending motions while destabilizing the top-down buoyancy-generated convection from the radiative cooling of air parcels above. However, this heating profile occurs only for a large fraction of total cloud LWP above the inversion base, which may not exist in reality.

The longwave radiative differences at the surface and TOA for cloud liquid above inversion base relative to the CCI case (factor 0) are shown in Fig. 16. For the observed $LWP = 65 \text{ g m}^{-2}$, we find that the longwave signature of such a cloud regime at the surface results in a decreased flux by up to 0.25 W m^{-2} relative to the canonical CCI regime (Fig. 16a). The cloud layer is opaque in the longwave, and redistribution of liquid above the inversion only increases the effective emission height. The TOA flux, however, is potentially largely enhanced, resulting in an increase in outgoing longwave radiation of up to 10 W m^{-2} (Fig. 16b) due to the higher effective emission temperature. Such a large TOA forcing range indicates a significant potential climate impact from the CII regime.

Decreasing the total cloud LWP can result in an increased surface longwave flux of approximately 1.5 W m^{-2} (Fig. 16a). These sensitivity tests suggest that, as total cloud optical thickness decreases, the enhanced flux associated with the warmer emission temperature above the inversion is able to penetrate through the optically thinner cloud. At the TOA, as LWP decreases, so does the change in outgoing longwave radiation. However, the effective emission height and temperature are still higher relative to the same cloud capped by the inversion, and thus the forcing remains positive. It is important to note that the forcing magnitudes in Fig. 16 are hypothetical and not universal. They will vary with the thermodynamic profile, cloud LWC distribution, and size of the droplets. However, the sign of the forcing is robust, based on longwave radiative transfer principles.

7. Discussion and summary

The relationship between low clouds and temperature inversions from three Arctic observation sites has been examined. We have emphasized the unique collocation

of cloud tops and temperature inversions, and have distinguished between the two cloud–inversion regimes defined in Sedlar and Tjernström (2009). We find the dominant cloud regime over sea ice–based observatories to be the cloud inside inversion (CII) regime, whereas observations from land are dominated by the cloud capped by inversion (CCI) regime. Analysis of the corresponding thermodynamic structures indicates that 2° – 4°C stronger and 200–300-m deeper inversions were more frequent with the CII regime. This regime also contained 200–400-m lower cloud-base and cloud-top heights relative to the CCI regime. Inversions associated with CCI cases were relatively weaker, often with strengths below 2°C . Sedlar and Tjernström find similar thermodynamic characteristics with data from a different sea-ice-based observatory. Thus, the thermodynamic structure appears to support the segregation into cloud regimes.

The layer between the surface and cloud base, the subcloud layer, tends to be statically unstable nearest the surface but transitions toward static stability in the middle of the layer. Similar stability profiles were estimated by Curry (1983) through an explanation on air-mass modification via radiation, turbulence, and cloud processes. This is found for all locations and cloud regimes except for CCI at Barrow. The presence of a stable layer indicates potential decoupling between the cloud base and subcloud layer, neglecting any mechanical forcing or strong updrafts, which might promote mixing. Similar decoupling is observed in the thermodynamics associated with a diurnal cycle in subtropical marine stratocumulus, as well as drizzling stratocumulus; however, these clouds generally flourish in a neutral or well-mixed layer with the ocean surface being a moisture source (e.g., Paluch and Lenschow 1991; Stevens et al. 1998). Arctic cloud layers, however, are found to be less statically stable for the CII regimes, and a thin portion of the subcloud layer below cloud base reflects this mixing potential. Therefore, even in cases when the surface is not providing heat and moisture to the cloud, the cloud has generated vertical motions that encompass at least the depth of the cloud and likely extend below cloud base. The presence of snow and sea ice are important physical properties of the Arctic, reducing the potential for cloud–subcloud–surface coupling via reduced sensible heat flux between surface and atmosphere. Ice and drizzle precipitation were identified in the cloud radar profiles as well as our simple precipitation metric described above. We find that reflectivities in the subcloud layer diminish close to the surface, indicating sublimation and evaporation. The latent heat released from these processes acts to stabilize the subcloud layer to cloud-top-generated vertical mixing (Stevens et al. 1998; Harrington et al. 1999), further suggesting that cloud

and precipitation processes at least partially determine the thermodynamic structure. Although the depletion of cloud water via drizzle may be small compared to the sources of cloud water (Herman and Goody 1976), we argue that ice and drizzle are important limiters of potential cloud LWC and subcloud stability (e.g., Curry 1983).

The presence of strong temperature and moisture inversions near cloud top suggests that the variable advection of heat and moisture is another key mechanism in promoting the cloud regimes. Moisture inversions occurred for more than 85% of the CII cases. Particularly in cases of decoupling between cloud and surface, the source of moisture to the cloud must be aloft and not at or near the surface as in subtropical stratus. Thus, the vertical advection of moisture appears necessary to maintain the cloud layer, while horizontal advection must be the ultimate source of the moisture aloft (e.g., Curry 1983; Curry et al. 1997; Pinto 1998). Horizontal advection at different vertical levels may also be partially responsible for stability between the surface and cloud layer. Such advection also leads to differences in positive gradients of the temperature and moisture inversions associated with the two cloud regimes. Stronger increases in the temperature gradient, where moisture is also observed to increase, will be necessary through advection in the presence of cloud cooling by longwave radiation. Since the rate of condensation is proportional to the rate of equivalent potential temperature change (Herman and Goody 1976), the potential for cloud maintenance above the inversion base in enhanced where temperature and moisture increases are largest.

Radar analysis indicates the predominant presence of liquid droplets near cloud top for both cloud regimes. Cloud-top longwave cooling depends on the vertical distribution of LWC. As hypothetically modeled here, the redistribution of a fraction of total LWC above the inversion base changes the effective cloud emissivity profile. Radiative cooling is distributed over a greater cloud depth when the cloud top occurs above the inversion base relative to when it occurs at the inversion base. However, the redistribution of cloud-top cooling does not suggest an increased occurrence of cloud dissipation or layering, suggested by Herman and Goody (1976), as the CII regime was the most frequent regime over sea ice. Instead, the redistribution over a larger depth may in fact increase the total cloud-layer cooling as proposed by Curry (1983) because longwave emissivity changes, promoting cloud condensate. Additionally, longwave radiative transfer modeling results suggest that the smaller longwave cooling rates associated with liquid above the inversion base will not necessarily force an adjustment of the thermodynamic profile. As demonstrated by the LWC profiles labeled 0.3 and 0.5 in Fig. 15,

the associated longwave cooling rates remain largest in the vicinity of the coldest level of the profile—the inversion base. Thus, the relatively smaller cooling rates near cloud top are less likely to force buoyant overturning in that region. This cooling may then directly force condensation (e.g., Curry 1983; Solomon et al. 2011), particularly when a moisture inversion is present. These processes are clearly dependent on the vertical distribution of cloud water near the cloud top and in relation to the inversion. In the future, we plan to use in situ measurements of cloud LWC and cloud-resolving models to better understand this distribution.

We are unable to definitively identify the reason for cloud segregation into one of two cloud regimes identified here. However, we have identified a number of processes specific to the Arctic that might promote cloud development within temperature inversions. We have also demonstrated that clouds extending into temperature inversions, which appear to be common, can significantly alter the radiative effects of these clouds relative to those that are capped by the inversion. This cloud structure can increase the surface longwave flux by as much as 1.5 W m^{-2} . Interestingly, the magnitude of enhanced surface longwave flux is similar to that observed when cloud-droplet effective radius is reduced to simulate increased aerosol loading in the Arctic (Garrett and Zhao 2006; Lubin and Vogelmann 2006). The impact on the TOA outgoing longwave flux is found to be a significant increase on the order of a few, and potentially up to 10, watts per square meter. These differences can therefore be considered climatologically important in the Arctic—particularly over the Arctic sea ice where the CII regime occurs more frequently than the canonical CCI regime. This unique cloud and thermodynamic relationship deserves further modeling attention to determine the capacity of current model parameterizations to capture this climatologically important mechanism of Arctic low-level clouds.

Acknowledgments. The authors wish to thank the anonymous reviewers for their constructive feedback. JS and MT were supported by the Swedish Research Council, the European Union 6th Framework program DAMOCLES, the Knut and Alice Wallenberg Foundation, and the Swedish Polar Research Secretariat. MS was supported by the U.S. National Science Foundation (ARC0732925, ARC1023366) and the Office of Science (BER), U.S. Department of Energy (DE-FG02-05ER63965). Observational data used in this study were provided by the Department of Energy Atmospheric Radiation Measurement Program, the NOAA/Earth System Research Laboratory, the SHEBA Project Office

at the University of Washington, and the ASCOS Program Office at Stockholm University.

REFERENCES

- Clothiaux, E. E., T. P. Ackerman, G. G. Mace, K. P. Moran, R. T. Marchand, M. Miller, and B. E. Martner, 2000: Objective determination of cloud heights and radar reflectivities using a combination of active remote sensors at the ARM CART sites. *J. Appl. Meteor.*, **39**, 645–665.
- Curry, J., 1983: On the formation of continental polar air. *J. Atmos. Sci.*, **40**, 2278–2292.
- , 1986: Interactions among turbulence, radiation and microphysics in Arctic stratus clouds. *J. Atmos. Sci.*, **43**, 90–106.
- , 1995: Interactions among aerosols, clouds and climate of the Arctic Ocean. *Sci. Total Environ.*, **160–161**, 777–791.
- , and E. E. Ebert, 1992: Annual cycle of radiation fluxes over the Arctic Ocean: Sensitivity to cloud optical properties. *J. Climate*, **5**, 1267–1280.
- , W. B. Rossow, D. Randall, and J. L. Schramm, 1996: Overview of Arctic Cloud and radiation characteristics. *J. Climate*, **9**, 1731–1764.
- , J. O. Pinto, T. Benner, and M. Tschudi, 1997: Evolution of the cloudy boundary layer during the autumnal freezing of the Beaufort Sea. *J. Geophys. Res.*, **102**, 13 851–13 860.
- Devasthale, A., U. Willén, K.-G. Karlsson, and C. G. Jones, 2010: Quantifying the clear-sky temperature inversion frequency and strength over the Arctic Ocean during summer and winter seasons from AIRS profiles. *Atmos. Chem. Phys.*, **10**, 5565–5572.
- Dong, X., B. Xi, K. Crosby, C. N. Long, R. S. Stone, and M. D. Shupe, 2010: A 10 year climatology of Arctic cloud fraction and radiative forcing at Barrow, Alaska. *J. Geophys. Res.*, **115**, D17212, doi:10.1029/2009JD013489.
- Frisch, A. S., C. W. Fairall, and J. B. Snider, 1995: Measurement of stratus cloud and drizzle parameters in ASTEX with a K-band Doppler radar and a microwave radiometer. *J. Atmos. Sci.*, **52**, 2788–2799.
- Garrett, T. J., and C. Zhao, 2006: Increased Arctic cloud longwave emissivity associated with pollution from mid-latitudes. *Nature*, **440**, 787–789.
- , L. F. Radke, and P. V. Hobbs, 2002: Aerosol effects on cloud emissivity and surface longwave heating in the Arctic. *J. Atmos. Sci.*, **59**, 769–778.
- Harrington, J. Y., T. Reisin, W. R. Cotton, and S. M. Kreidenweis, 1999: Cloud resolving simulations of Arctic stratus. Part II: Transition-season clouds. *Atmos. Res.*, **51**, 45–75.
- Herman, G., and R. Goody, 1976: Formation and persistence of summertime Arctic stratus clouds. *J. Atmos. Sci.*, **33**, 1537–1553.
- Intrieri, J. M., C. W. Fairall, M. D. Shupe, P. O. G. Persson, E. L. Andreas, P. S. Guest, and R. E. Moritz, 2002a: An annual cycle of Arctic surface cloud forcing at SHEBA. *J. Geophys. Res.*, **107**, 8039, doi:10.1029/2000JC000439.
- , M. D. Shupe, T. Uttal, and B. J. McCarty, 2002b: An annual cycle of Arctic cloud characteristics observed by radar and lidar at SHEBA. *J. Geophys. Res.*, **107**, 8030, doi:10.1029/2000JC000423.
- Kahl, J. D., 1990: Characteristics of the low-level temperature inversion along the Alaskan Arctic coast. *Int. J. Climatol.*, **10**, 537–548.
- Klein, S. A., and D. L. Hartmann, 1993: The seasonal cycle of low stratiform clouds. *J. Climate*, **6**, 1587–1606.
- Liu, Y., J. R. Key, A. Schweiger, and J. Francis, 2006: Characteristics of satellite-derived clear-sky atmospheric temperature inversion strength in the Arctic, 1980–96. *J. Climate*, **19**, 4902–4913.
- Lubin, D., and A. M. Vogelmann, 2006: A climatologically significant aerosol longwave indirect effect in the Arctic. *Nature*, **439**, 453–456.
- Minnett, P. J., 1999: The influence of solar zenith angle and cloud type on cloud radiative forcing at the surface in the Arctic. *J. Climate*, **12**, 147–158.
- Mlawer, E. J., S. J. Taubman, P. D. Brown, M. J. Iacono, and S. A. Clough, 1997: Radiative transfer for inhomogeneous atmospheres: RRTM, a validated correlated-k model for the longwave. *J. Geophys. Res.*, **102**, 16 663–16 682.
- Moran, K. P., B. E. Martner, M. J. Post, R. A. Kropfli, D. C. Welsh, and K. B. Widener, 1998: An unattended cloud-profiling radar for use in climate research. *Bull. Amer. Meteor. Soc.*, **79**, 443–455.
- Paluch, I. R., and D. H. Lenschow, 1991: Stratiform cloud formation in the marine boundary layer. *J. Atmos. Sci.*, **48**, 2141–2158.
- Pinto, J. O., 1998: Autumnal mixed-phase cloudy boundary layers in the Arctic. *J. Atmos. Sci.*, **55**, 2016–2038.
- Pruppacher, H. R., and J. D. Klett, 1997: *Microphysics of Clouds and Precipitation*. Kluwer Academic Publishers, 954 pp.
- Sedlar, J., and M. Tjernström, 2009: Stratiform cloud—Inversion characterization during the Arctic melt season. *Bound.-Layer Meteorol.*, **132**, 455–474.
- , and Coauthors, 2011: A transitioning Arctic surface energy budget: The impacts of solar zenith angle, surface albedo and cloud radiative forcing. *Climate Dyn.*, **37**, 1643–1660.
- Serreze, M. C., J. D. Kahl, and R. C. Schnell, 1992: Low-level temperature inversions of the Eurasian Arctic and comparisons with Soviet drifting stations. *J. Climate*, **5**, 615–630.
- Shupe, M. D., 2011: Clouds at Arctic atmospheric observatories. Part II: Thermodynamic phase characteristics. *J. Appl. Meteor. Climatol.*, **50**, 645–661.
- , and J. M. Intrieri, 2004: Cloud radiative forcing of the Arctic surface: The influence of cloud properties, surface albedo, and solar zenith angle. *J. Climate*, **17**, 616–628.
- , T. Uttal, S. Y. Matrosov, and A. S. Frisch, 2001: Cloud water contents and hydrometeor sizes during the FIRE Arctic Clouds Experiment. *J. Geophys. Res.*, **106**, 15 015–15 028.
- , P. Kollias, S. Y. Matrosov, and T. L. Schneider, 2004: Deriving mixed-phase cloud properties from Doppler radar spectra. *J. Atmos. Oceanic Technol.*, **21**, 660–670.
- , T. Uttal, and S. Y. Matrosov, 2005: Arctic cloud microphysics retrievals from surface-based remote sensors at SHEBA. *J. Appl. Meteor.*, **44**, 1544–1562.
- , S. Y. Matrosov, and T. Uttal, 2006: Arctic mixed-phase cloud properties derived from surface-based sensors at SHEBA. *J. Atmos. Sci.*, **63**, 697–711.
- , P. Kollias, P. O. G. Persson, and G. M. McFarquhar, 2008a: Vertical motions in Arctic mixed-phase stratiform clouds. *J. Atmos. Sci.*, **65**, 1304–1322.
- , —, M. Poellot, and E. Eloranta, 2008b: On deriving vertical air motions from cloud radar Doppler spectra. *J. Atmos. Oceanic Technol.*, **25**, 547–557.
- , V. P. Walden, E. Eloranta, T. Uttal, J. R. Campbell, S. M. Starkweather, and M. Shiobara, 2011: Clouds at Arctic atmospheric observatories. Part I: Occurrence and macrophysical properties. *J. Appl. Meteor. Climatol.*, **50**, 626–644.
- Solomon, A., M. D. Shupe, P. O. G. Persson, and H. Morrison, 2011: Moisture and dynamical interactions maintaining decoupled Arctic mixed-phase stratocumulus in the presence of a humidity inversion. *Atmos. Chem. Phys.*, **11**, 10 127–10 148.

- Stephens, G. L., 1978: Radiation profiles in extended water clouds. II: Parameterization schemes. *J. Atmos. Sci.*, **35**, 2123–2132.
- Stevens, B., W. R. Cotton, G. Feingold, and C.-H. Moeng, 1998: Large-eddy simulations of strongly precipitating, shallow, stratocumulus-topped boundary layers. *J. Atmos. Sci.*, **55**, 3616–3638.
- Tjernström, M., and A. Rune, 2003: The turbulence structure of stratocumulus during the ASTEX first Lagrangian experiment. *Quart. J. Roy. Meteor. Soc.*, **129**, 1071–1100.
- , and R. G. Graversen, 2009: The vertical structure of the lower Arctic troposphere analysed from observations and ERA-40 reanalysis. *Quart. J. Roy. Meteor. Soc.*, **135**, 431–443.
- , C. Leck, P. O. G. Persson, M. L. Jensen, S. P. Oncley, and A. Targino, 2004: The summertime Arctic atmosphere: Meteorological measurements during the Arctic Ocean Experiment 2001. *Bull. Amer. Meteor. Soc.*, **85**, 1305–1321.
- Tsay, S. C., and K. Jayaweera, 1984: Physical characteristics of Arctic stratus clouds. *J. Climate Appl. Meteor.*, **23**, 584–596.
- Uttal, T., and Coauthors, 2002: Surface heat budget of the Arctic Ocean. *Bull. Amer. Meteor. Soc.*, **83**, 255–275.
- Wang, X., and J. R. Key, 2005: Arctic surface, cloud, and radiation properties based on the AVHRR Polar Pathfinder dataset. Part I: Spatial and temporal characteristics. *J. Climate*, **18**, 2558–2574.
- Westwater, E. R., Y. Han, M. D. Shupe, and S. Y. Matrosov, 2001: Analysis of integrated cloud liquid and precipitable water vapor retrievals from microwave radiometers during SHEBA. *J. Geophys. Res.*, **106**, 15 099–15 112.
- Zuidema, P., and Coauthors, 2005: An Arctic springtime mixed-phase cloudy boundary layer observed during SHEBA. *J. Atmos. Sci.*, **62**, 160–176.